Available online at www.sciencedirect.com
ScienceDirect
Trans. Nonferrous Met. Soc. China 35(2025) 1281−1291

Transactions of Nonferrous Metals Society of China
www.tnmsc.cn

Mechanisms of ductile-to-brittle transition in Sn−3.0Ag−0.5Cu solder alloy at cryogenic temperature

Sheng-li LI[1], Chun-jin HANG[1,2], Qi-long GUAN[1], Xiao-jiu TANG[1],
Ning ZHOU[1], Yan-hong TIAN[1], Wei ZHANG[1], Dan YU[3], Ying DING[3], Xiu-li WANG[3]

1. State Key Laboratory of Precision Welding & Joining of Materials and Structures,
Harbin Institute of Technology, Harbin 150001, China;
2. Zhengzhou Research Institute, Harbin Institute of Technology, Zhengzhou 450041, China;
3. Beijing Institute of Control Engineering, Beijing 100094, China

Received 25 August 2023; accepted 10 May 2024

Abstract: The inherent brittle behavior and ductile-to-brittle transition (DBT) mechanism of Sn−3.0Ag−0.5Cu (SAC305) solder alloy at the liquid nitrogen temperature (LNT, 77 K) were investigated through uniaxial tensile experiments conducted at different temperatures. Dynamic recovery and recrystallization of SAC305 solder alloy at room temperature (RT, 293 K) activate a softening process. Conversely, intersecting and none-intersecting deformation twins, embedded in body-centered tetragonal Sn, enhance tensile strength and stabilize strain hardening rate, while suppressing the elongation of the alloy at LNT. The irreconcilable velocity difference between twin thickening (~8 μm/s) and dislocation slip (~4 μm/s) results in premature brittle fracture, during the linear hardening and DBT. Moreover, the secondary phases degrade the mechanical property of SAC305 solder alloy, and micro-cracks appear between Cu_6Sn_5 and Ag_3Sn in the eutectic matrix.

Key words: SAC305; deformation twinning; secondary phases; tensile property; cryogenic temperature

---

1 Introduction

Sn-based solders offer the electrical and mechanical connections between the chip and the pad as well as between the component (encapsulated chip) and the printed circuit board (PCB) [1]. Sn−3.0Ag−0.5Cu (SAC305) lead-free solder has been applied in modern electronic manufacturing [2,3]. Due to its excellent wetting behaviors and chemical characteristics, the alloy assemblies can absorb high stress [3]. Once the ambient temperature decreases to extreme temperature state, SAC305 solder alloy requires extremely high reliability [4]. In addition, SAC305 eutectic alloy incorporate 96.5% Sn [5] and Sn with body-centered tetragonal (BCT) structure leads to a ductile-to-brittle transition (DBT) at cryogenic temperature [6]. The DBT of the solder alloy often triggers the failure of electronics at low temperature [3]. Thus, it is a potentially threaten for those electronics, which survive and operate at extreme temperature, for instance, on Giant Planets (−140 °C) [6], Mars (−140 °C) [6] and Moon (down to −196 °C) [7].

The brittle fracture of SAC305 solder alloy has been investigated at extreme temperature [8,9]. Most of the investigations about the mechanical behavior of SAC305 solder alloy were conducted only above 218 K [7,9−11]. It is generally accepted that twins can allow a large plastic deformation rather than lead to brittleness [12,13]. Deformation

---

Corresponding author: Chun-jin HANG, Tel: +86-451-86418359, E-mail: hangcj@hit.edu.cn;
Wei ZHANG, E-mail: zhangw@hit.edu.cn

DOI: https://doi.org/10.1016/S1003-6326(24)66748-8

twinning occurs as a dominant deformation mechanism and thus remains unclear. In this work, we carried out uniaxial tensile experiments with a large strain rate of 0.01 s^{-1} on SAC305 solder alloy to clarify the cryogenic deformation performances before brittle fracture and further elucidate the DBT mechanism. The precise mechanism can be helpful in designing Sn-based solders and joints with modified mechanical behavior and embrittlement resistance for cryogenic electronics.

2 Experimental

2.1 Materials and mechanical testing

Commercially SAC305 solder alloy contains a large concentration of Sn (>95%) with a BCT crystal structure, and the rectangular dog-bone shaped tensile samples were fabricated from the cast slabs by wire electrical discharge machining. The tensile specimens with a gauge dimensions of 60 mm (length, rolling direction, RD) × 15 mm (width, transverse direction, TD) × 3 mm (thickness, normal direction, ND) were applied to in-situ uniaxial tensile experiments. The experimental processes of the cryogenic tensile test are shown in Fig. 1. The dog-bone shape specimens were immersed in a liquid nitrogen environment for 30 min and then stretched at a strain rate of 0.01 s^{-1}.

2.2 Microstructure characterizations

The microstructures were analyzed using an SEM−EBSD technique with orientation imaging microscopy (OIM) software on the surface of tensile specimens deformed at different temperatures. Tensile specimens were electro-polished in a mixture of perchloric acid and acetic with 1:9 in volume ratio for EBSD characterizations under scanning electron microscope. The electron beam energy and the scanning step size were set to be 30 kV and 1 μm, respectively. The fracture morphologies of tensile specimens were observed by scanning electron microscope (SEM, FEI, Quanta 200 FEG). Thin SAC305 foil was fabricated using a focused ion beam (FIB, FEI Helios NanoLab 600i) by cutting through the typical twin boundaries (TBs) that were observed from EBSD analysis. A transmission electron microscope (TEM, Talos F200x) was employed to examine twinning information.

3 Results

3.1 Mechanical performances at LNT and RT

Figure 2(a) shows the initial microstructure of SAC305 solder alloy, which consists of β-Sn and eutectic microstructure (Ag$_3$Sn and Cu$_6$Sn$_5$). The engineering stress−strain curves of SAC305 solder alloy at LNT and RT are shown in Fig. 2(b). The solder alloy at RT displays yield strength (YS, 0.2% engineering strain, $\approx\sigma_Y$) of 25.5 MPa, tensile strength (TS) of 51.6 MPa, and a total elongation (EL) of 56.5%. The YS (46.2 MPa) and TS (81.8 MPa) of SAC305 solder alloy at LNT is higher than those of the alloy at RT. However, EL changes from 56.5% (RT) to 6.9% (LNT). As the ambient temperature declines from 293 to 77 K, the alloy at LNT exhibits the brittle fracture behavior. The DBT mechanism and fracture feature of SAC305 solder alloy at LNT are explored by analyzing the strain hardening behaviors. The stress−strain carves are used to response the strain hardening behavior and calculate the strain hardening rate (Figs. 2(c, d)). In the LNT case, the strain hardening carves of SAC305 solder alloy exhibit two stages. The first stage shows a continuous decrease in (dσ/dε)/G and the second stage remains at a nearly constant hardening rate. The linear stage promotes a continues increase in

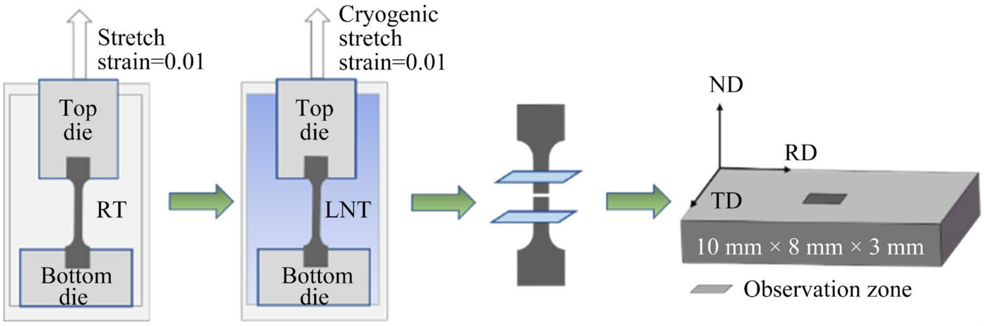

Fig. 1 Schematic diagram of deformation process

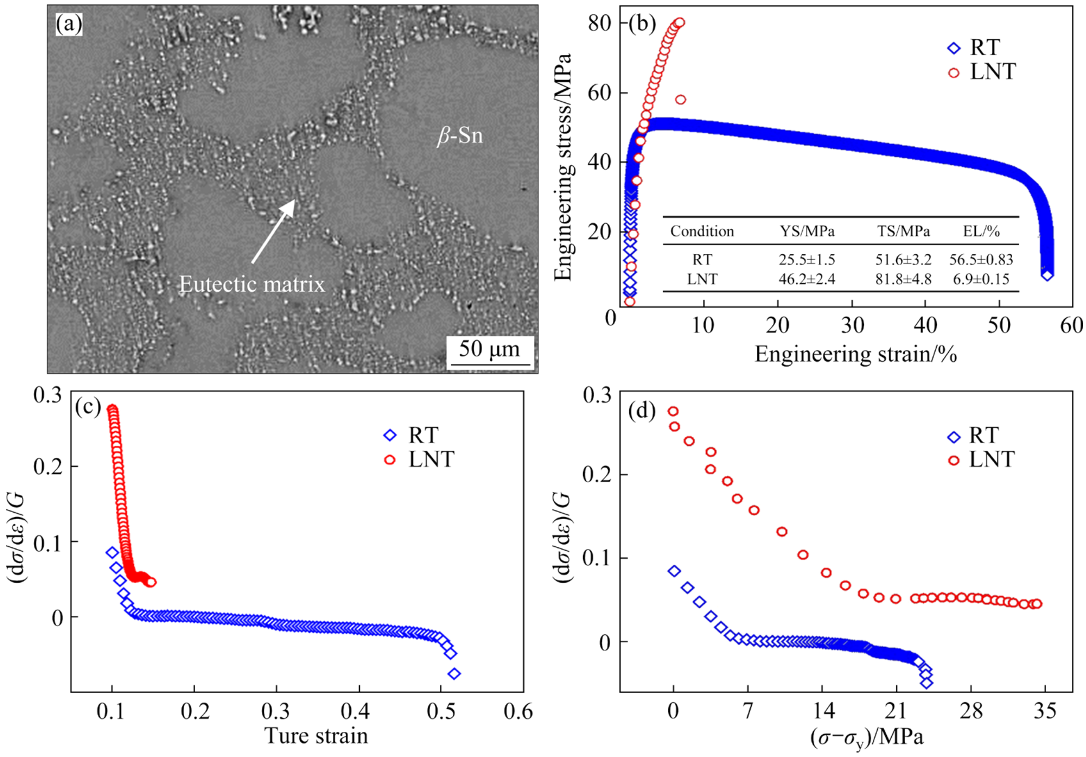

Condition	YS/MPa	TS/MPa	EL/%
RT	25.5±1.5	51.6±3.2	56.5±0.83
LNT	46.2±2.4	81.8±4.8	6.9±0.15

Fig. 2 SEM image of specimen before tensile (a); Engineering stress−strain curves of SAC305 alloy (b); Normalized true strain hardening rates by shear modulus ($(\mathrm{d}\sigma/\mathrm{d}\varepsilon)/G$) plotted as function of true strain (c) and flow stress ($\sigma-\sigma_y$) (d)

the material strength, but terminates with a sudden rupture at 0.056 true strain (Fig. 2(c)). Noticeably, $(\mathrm{d}\sigma/\mathrm{d}\varepsilon)/G$ values of SAC305 solder alloy at RT is much lower than that of the alloy at LNT during deformation process. In the RT case, the strain hardening behavior of the alloy consists of three stages. As shown in Fig. 2(d), the initial stage of $(\mathrm{d}\sigma/\mathrm{d}\varepsilon)/G$ ends at 6.62 MPa of $(\sigma-\sigma_0)$. $(\mathrm{d}\sigma/\mathrm{d}\varepsilon)/G$ values of SAC305 solder alloy approach zero and subsequent become negative in the second stage.

3.2 Fracture morphologies at LNT and RT

Fracture morphologies of SAC305 solder alloy provide proofs to fracture initiation and propagation and thus help elaborate the fracture mechanism with decreasing the temperature. Figure 3 displays the tensile fracture morphologies obtained at LNT and RT. As presented in Fig. 3(a), overall fracture fractography after ductile fracture at RT exhibits dimples. Figure 3(c) shows the tensile fracture morphologies of SAC305 solder alloy at LNT. Cracks and some granular textures are observed on the intergranular fracture surface (Figs. 3(d, e)). It can be found that the granular texture is fracture result of the eutectic structure. Moreover, a small fraction of transgranular fractures are observed on the fracture surface (Fig. 3(f)).

3.3 Microstructure evolution at RT and LNT

In this work, the microstructure of SAC305 specimens after brittle fracture at low temperature was observed under optical microscopy (OM). Figure 4 shows the microstructure evolution of the alloy during deformation process. It can be found from Fig. 4(a) that β-Sn and eutectic microstructure on the surface are clearly visible. As the true strain (ε_T) increases to 0.015, tiny cracks are observed on the fracture surface, and mainly locate at the grain boundaries (GBs) of β-Sn. In addition, a large crack initiates from the edge of SAC305 sample (Fig. 4(b)). The strain accumulation reinforces the continuous expansion of cracks in the β-Sn regions (Figs. 4(c−e)). Based on the above phenomena, in-situ tensile experiment of the solder alloy confirms that cracks initially occur at the edge of β-Sn and then propagate to the eutectic microstructure (see Section 1 in Supplementary Information).

The EBSD technique was used to analyze the surface of SAC305 solder alloy. Figure 5 shows the inverse pole figures (IPF) and misorientation

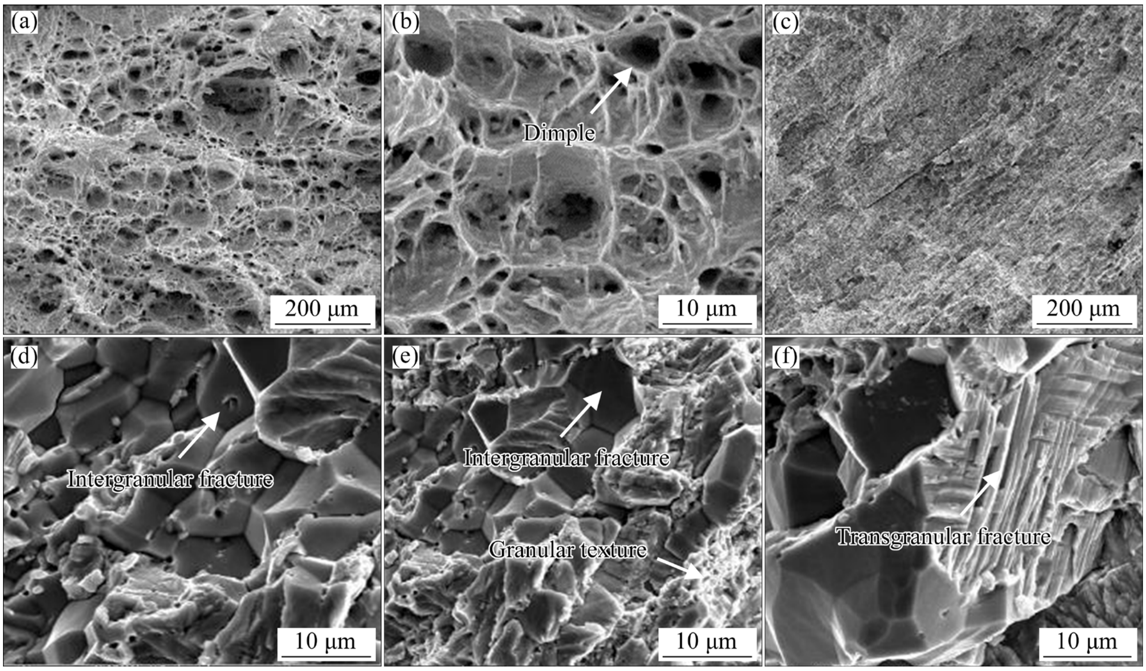

Fig. 3 SEM images of fractured SAC305 samples at RT and LNT: (a) Overall morphology obtained at RT; (b) Ductile fracture dimples at RT; (c) Brittle fracture surface at LNT; (d−f) Enlarged fracture surface at LNT

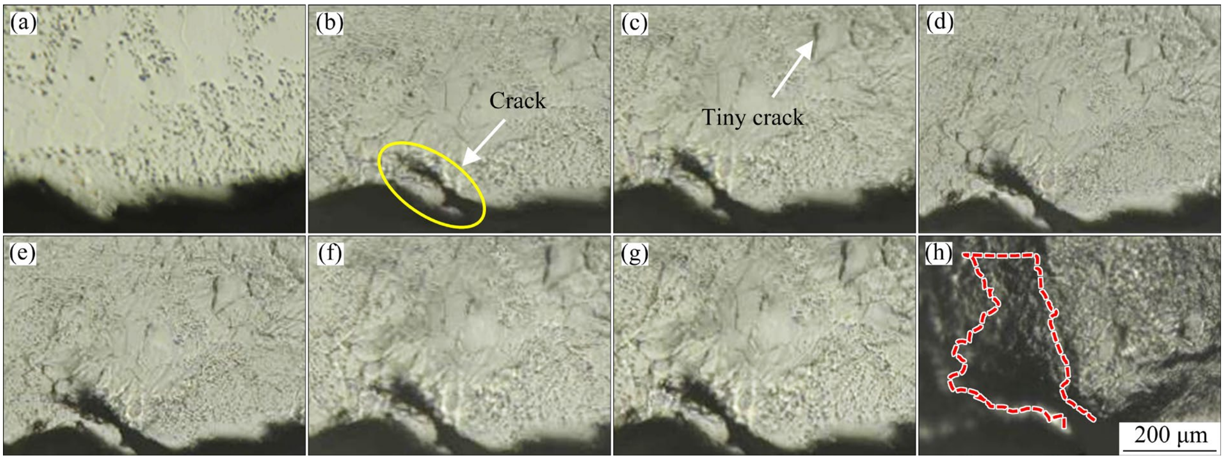

Fig. 4 Microstructure evolution of alloy for different strains at LNT: (a) ε_T=0; (b) ε_T=0.015; (c) ε_T=0.02; (d) ε_T=0.028; (e) ε_T=0.035; (f) ε_T=0.044; (g) ε_T=0.05; (h) ε_T=0.056

distributions for the crystal direction of the fractured specimens at LNT and RT. As displayed in Fig. 5, black and red lines represent high angle grain boundaries (HAGBs, misorientation angles >15°) and low angle grain boundaries (LAGBs, 2° < misorientation angles < 15°), respectively. Besides, blue lines are used to trace the boundaries with a specific misorientation of 60°(±5°) about ⟨100⟩ axis. According to twinning mode theory [9,14], {301} twins and {101} twins of BCT Sn are corresponding to the misorientations of 62.8°@⟨100⟩ and 57.2°@⟨100⟩, respectively. As shown in Fig. 5(a), the average grain size of SAC305 specimen is about 50 μm and the misorientation angle exhibits a relatively uniform distribution before tensile (Fig. 5(b)). Moreover, the LAGBs, which are typically located in the grain interiors, account for 75.3% (Table 1), and particularly, small misorientations (~2.98°) predominate at RT (Figs. 5(c, d)). These results indicate that dynamic recovery (DRV) and dynamic recrystallization (DRX), which are marked using black triangles in Fig. 5(c) with corresponding EBSD analysis seen in Section 2 in Supplementary Information, occur in the plastic deformation. The long zero-hardening stage is attributed to the DRV

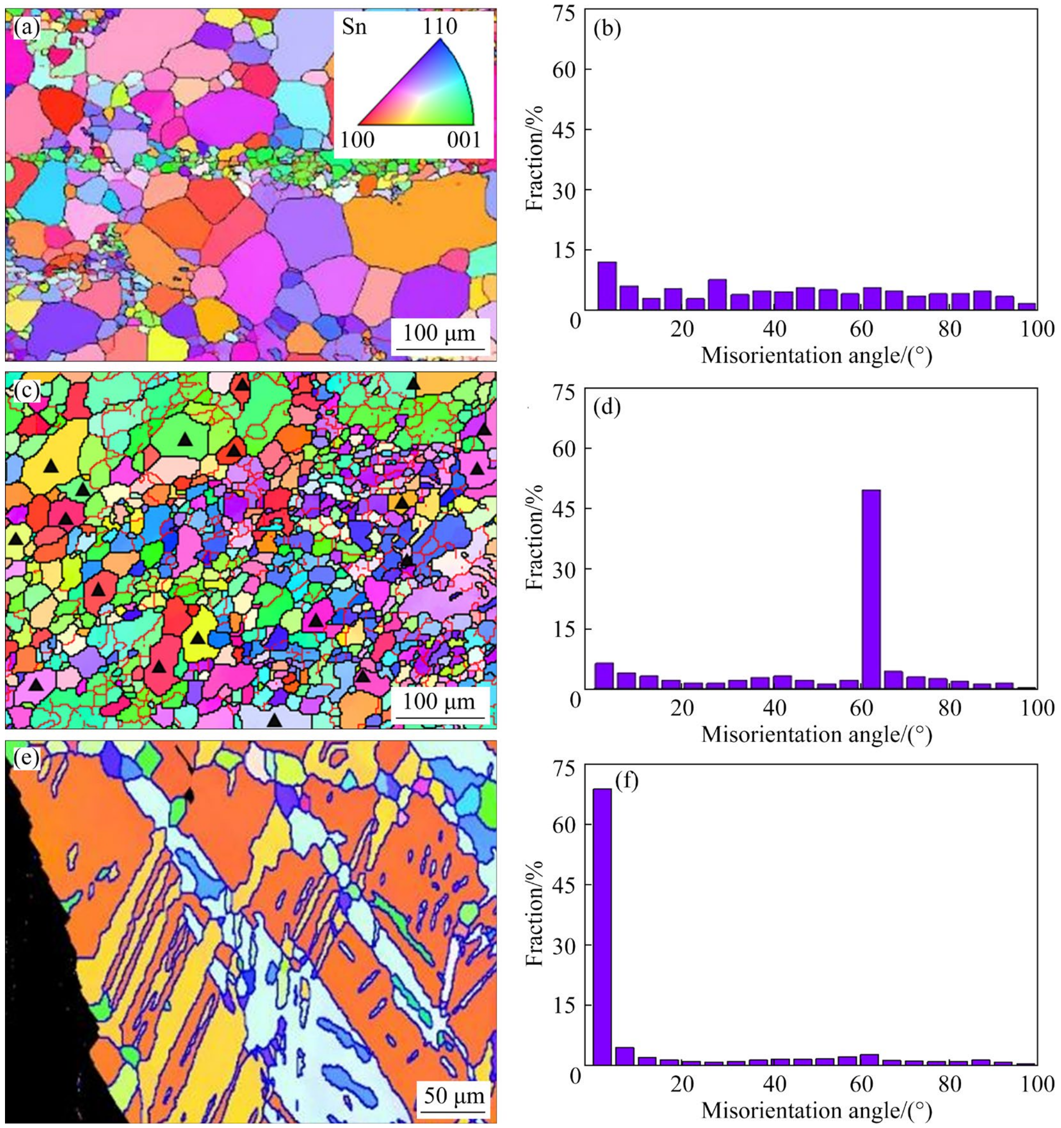

Fig. 5 IPF (a, c, e) and misorientation distributions (b, d, f) of SAC305 specimens: (a, b) As-prepared sample; (c, d) At RT; (e, f) At LNT

Table 1 Fraction of orientation distribution for LAGBs, HAGBs and 60°@⟨100⟩ GBs in Fig. 5

Sample	LAGB	HAGB	60°@⟨100⟩ GBs
As-prepared	15.6%	84.4%	9.9%
At RT	75.3%	24.7%	5.1%
At LNT	21.6%	78.4%	49.2%

and DRX, which implies GB sliding (grain rotation)-governed deformation (Fig. 2(c)) [14]. However, deformation twinning is totally restricted at RT (only 5.1% 60°@⟨100⟩ boundaries), as listed in Table 1. After the tensile fracture at LNT, the orientation of 60°@⟨100⟩ boundaries within individual grains account for 49.2% of all the boundaries (Table 1). These phenomena are consistent with the misorientation angle distribution of 62.8° for {301} deformation twin in Sn [15].

3.4 Deformation characterization at LNT

On the surface of the LNT tensile SAC305 sample, parallel Twins 2 with the 60°@[010] boundaries are formed within Matrix 1, and EBSD analysis is used to detect deformation twins (Fig. 6(a)). As presented in Fig. 6(b), the cells of Twins 2 and Matrix 1 are used to reflect the crystallographic relationship. According to the crystal reference frame [100]−[010]−[001], it is noticed that [010] axis of Twin 2 is parallel to [010] axis of Matrix 1. To further evaluate the crystallography relationship between Twin 2 and Matrix 1, {301}, {001}, {100}, {101} pole figures

(PFs) confirm the existence of common (301) twin plane, which is highlighted by the purple enclosed rectangle in Fig. 6(c). Figure 6(d) shows TEM image and diffraction spots image of thin foil. The high resolution TEM (HRTEM) images of matrix and twin exhibit two lattice stripes with spacings of 0.2046 and 0.2048 nm corresponding to the $(30\bar{2})_\beta$ and $(30\bar{2})_\beta$ planes, respectively (Fig. 6(e)). This asymmetry in atomic arrangement indicates the formation of edge dislocations along (301) TBs (Fig. 6(f)).

3.5 Intersecting twins at LNT

As shown in Fig. 7(a), there are three primary twins (T_1, T_2, T_3) inside the matrix (M) at LNT. Parallel {301} twins (T_2, T_3) grow and encounter with primary Twin T_1. T_2 and T_3 twins cross the original matrix and finally terminate at the border of Twin T_1. Such multiple intersecting relationships (Fig. 7(b)) between twins produce considerable intersections within the original matrix where a great number of dislocations are blocked. Therefore, high stress concentrations caused by dislocation accumulation occur around these intersections, as displayed by the high angles of kernel average misorientation (KAM) in Fig. 7(c).

3.6 Cracks analysis of alloy at LNT

When the temperature declines from RT to LNT, the fracture mode of SAC305 solder alloy varies from ductile fracture to brittle fracture. Fracture morphologies indicate that brittle cracks at LNT extend mainly in an intergranular mode (Fig. 3). A detailed EBSD analysis of microcracks along GBs (Fig. 8) shows a vital result that the cracked GBs intersect with the deformation twins (Figs. 8(b, c)). In-situ tensile test under OM further confirms that the brittle cracks initiate and extend

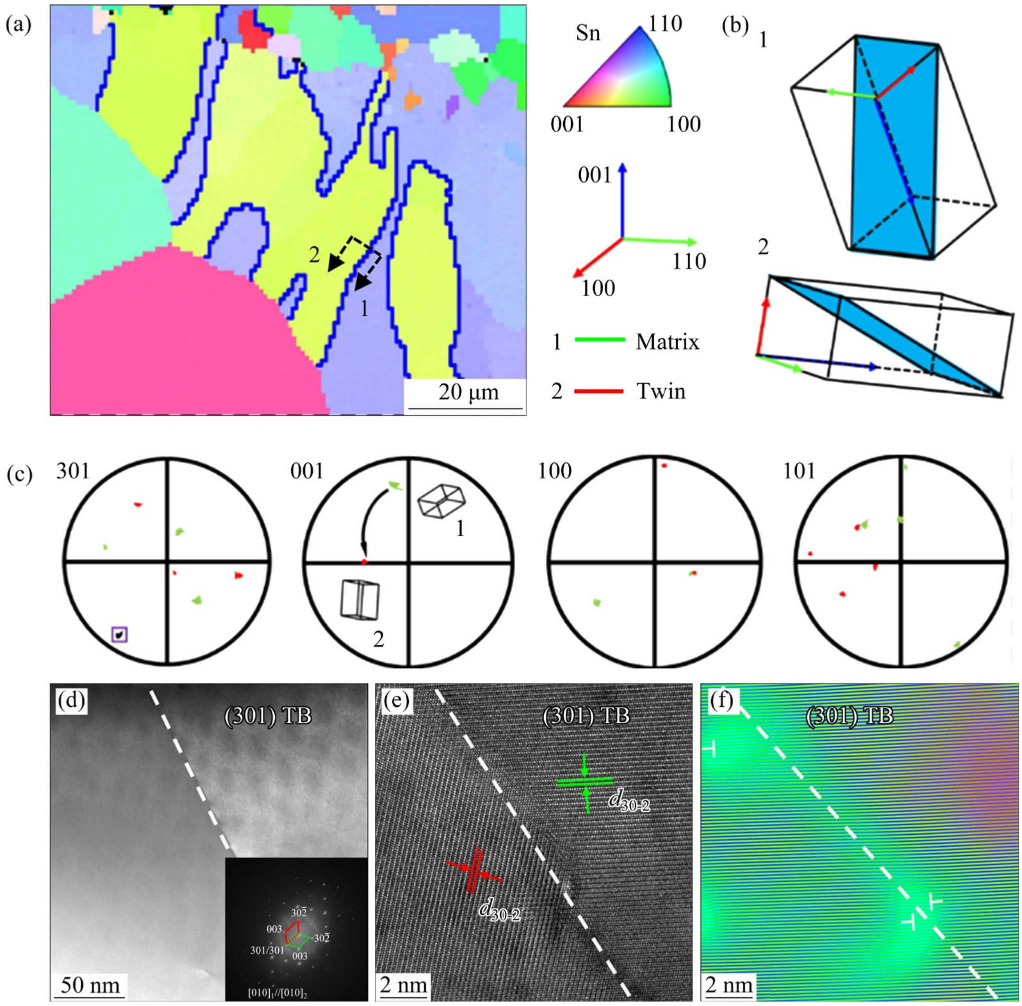

Fig. 6 IPF of lamella Twin 2 embedded within Matrix 1 (a); Schematic cell diagrams of Matrix 1 and Twin 2 (b); PFs of Matrix 1 and Twin 2 (c); TEM image and corresponding diffraction spots (d); HRTEM image (e); Filtered inverse FFT image (f)

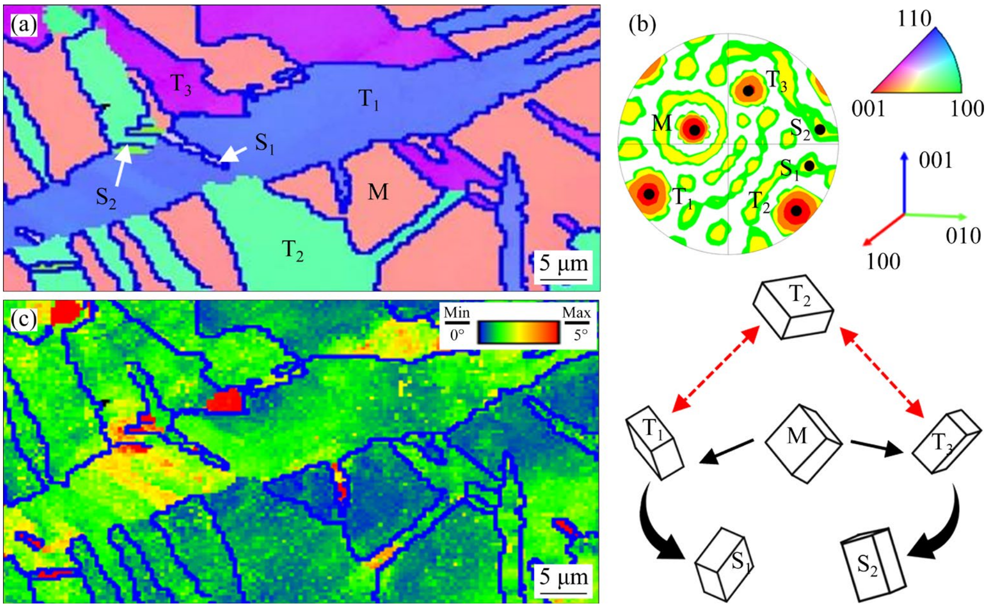

Fig. 7 IPF of twins and matrix (a); PF map and crystal orientation diagrams of twins and matrix (b); Corresponding KAM map (c)

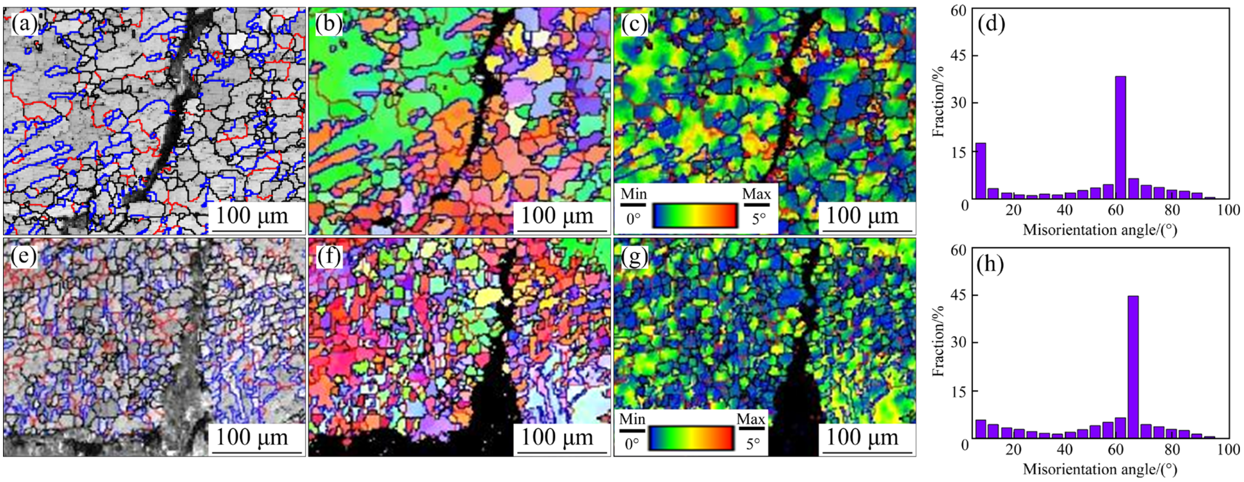

Fig. 8 SEM micrographs (a, e), IPF maps (b, f), KAM maps (c, g) and misorientation distribution (d, h) of alloy: (a−d) Internal crack; (e−h) Edge crack

along the twin−GB interactions at LNT (Fig. 4 and Fig. S1 in Supplementary Information). As shown in Fig. 8(c), KAM map of the interior crack with high stress distribution is displayed. In addition, the fraction of deformation twins is counted as 32.8% at LNT (Fig. 8(d)). Figures 8(e−h) depict the propagated crack of the unenclosed region corresponding to the in-situ tensile sample-fractured of Fig. 4. As shown Fig. 8(f), it can be found that the interaction between twin and GBs exists as the thickness of twin increases. According to the dynamic Hall−Petch effects [16,17], GBs decline the mean free path of the dislocation, which is hindered by the GBs [18]. These intersections promote the grain refinement and lead to the linear hardening of the alloy. High stress concentrations at these produced twin−twin intersections (Fig. 8(g)) indicate that there occurs a massive pile-up of dislocations.

4 Discussion

4.1 Strain hardening mechanism at LNT

To elaborate the brittle fracture of the alloy, it is necessary to elucidate the strain hardening mechanisms at LNT firstly. In the RT case, the hardening rate curve decreases to zero at ~0.03 of true strain, and the curve exhibits a long zero-hardening stage before fracture (Fig. 2). Different from RT case, the hardening rates undergo a monotonic decline and reach a transient hardening plateau (>0) with sudden fracture at ~0.056 of ture strain at LNT. EBSD analysis after fracture indicates that a great number of {301} deformation twins occur (Figs. 4 and 5). Therefore, the distinctive work hardening performances might be modulated by the different stages of deformation twinning. As proposed by some researchers [16,17], a strong interaction between slip and twinning as well as between the blocked twins has been observed. Intersecting twins can subdivide grains and further decline the dislocation mean free path [17]. These intersections therefore act as more effective deformation barriers to dislocation gliding and lead to this linear hardening (Fig. 2(c)). High KAM values at twin−GBs intersections suggest that a massive pile-up of dislocation exists (Figs. 7 and 8).

4.2 DBT mechanism of SAC305 solder alloy at LNT

When the ambient temperature reduces from RT to LNT, the fracture mechanism of SAC305 solder alloy transforms from ductile fracture to brittle fracture (Figs. 2 and 3). The fracture morphology of the alloy indicates that the brittle cracks at LNT extend mainly in an intergranular mode (Fig. 3). As shown in Fig. 8, EBSD technique is conducted to analyze the internal cracks on the fracture surface. In-situ uniaxial tensile result show that the brittle cracks initiate and propagate along the twin−GB intersections at LNT (see Fig. 4 and Section 1 in Supplementary Information). Accordingly, high stress distribution around these twin−GB intersections is identified from KAM map (Fig. 7(c)). It has been figured out that the occurrence of local stress concentration may be related to the strong interaction between deformation twins and dislocations. By considering that GBs are sheared by twin dislocations along the twinning direction (Fig. 4(a)), once shear strains cannot be accommodated by the plastic deformation in neighboring grains, local stress concentrations take place at these twin−GB intersections as the twins thicken (Fig. 4(c)). Once the concentrated stress exceeds the strength of GB, the GB will be pulled open to form a GB crack (Fig. 4(h)) [19]. Therefore, it can be concluded that the twin-induced GB failure is attributed to the velocity mismatch between twin growth and dislocation slip.

According to EBSD result, the average thickness of {301} twins at LNT is estimated to be 32.8 μm. When considering that {301} twins are activated at ~0.015 of true strain and fracture at ~0.056 of true strain (Fig. 2(c)), the average thickening rate of {301} twin can be calculated as 8 μm/s. According to the Taylor hardening model [17], the increase in shear stress ($\Delta\tau$) is described as follows:

$$\Delta\tau=\Delta\sigma/M=\alpha Gb\rho^{1/2} \tag{1}$$

where $\Delta\sigma$ is the increment of the tensile stress, M is the Taylor factor (1.43, See Section 3 in Supplementary Information), α represents a constant (0.5 [17,20,21]), G is the shear modulus (15 GPa [22,23]), b is the magnitude of the Burgers vector (0.37 nm [24,25]), and ρ is the dislocation density. Therefore, the dislocation density value ρ is calculated as $8.69\times10^{12}\ \mathrm{m}^{-2}$.

Based on the Orowan equation [26], the plastic shear rate $\dot{\gamma}$ is originated by the dislocation slip before the occurrence of deformation twin during tensile process:

$$\dot{\gamma}=M\dot{\varepsilon}=b\rho v_{\mathrm{d}} \tag{2}$$

where $\dot{\varepsilon}$ represents the strain rate. According to the Eq. (2), the dislocation slip velocity (v_{d}) can be estimated as 4 μm/s. Therefore, the dislocation slip velocity is only 50% of the twin thickening rate (8 μm/s).

Figure 9 show SEM/EBSD micrographs on the fracture surface of the alloy at LNT. As confirmed from the SEM/EBSD analysis in Fig. 9(a), microcracks are formed on the fracture surface. Cu_6Sn_5 and Ag_3Sn phases around microcracks are also detected (Figs. 9(b−d) and 10(c)). As proposed by previous studies [27,28], the secondary phases lead to the formation of microcracks in the soft microstructure. In addition, larger directional coefficient of thermal expansion (CTE) mismatch between Sn and the secondary phases containing Cu_6Sn_5 and Ag_3Sn contributes to the expansion of microcrack at cryogenic temperature [29−31]. Therefore, this phenomenon results in the propagation of cracks along the secondary phases.

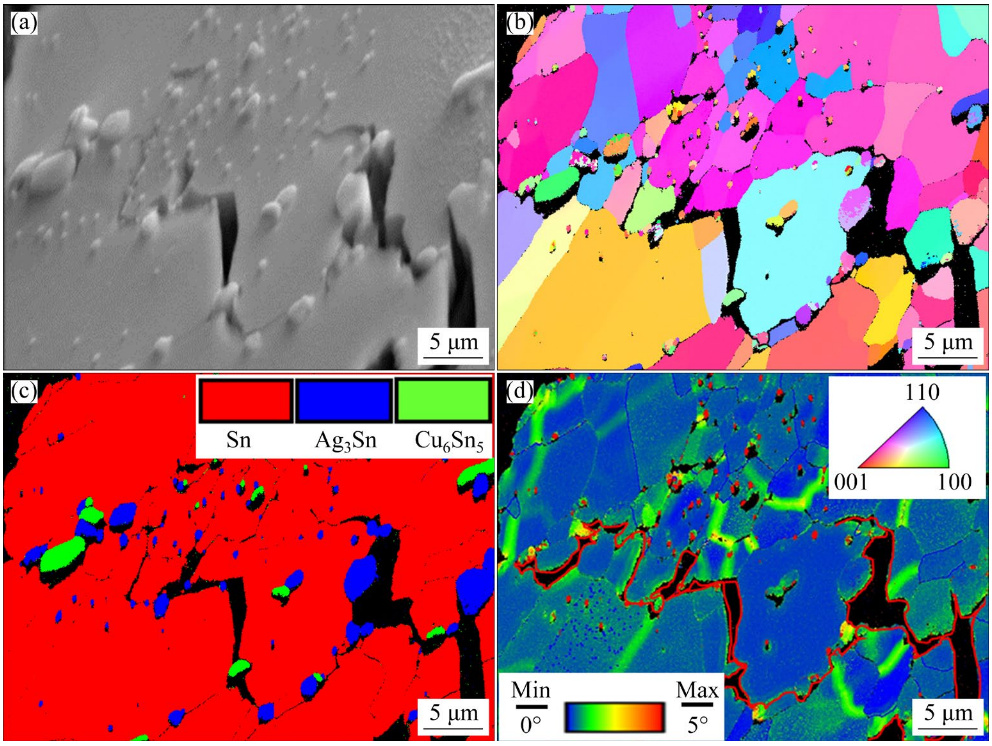

Fig. 9 SEM morphology (a), IPF map (b), phase map (c) and KAM map (d) of alloy at LNT

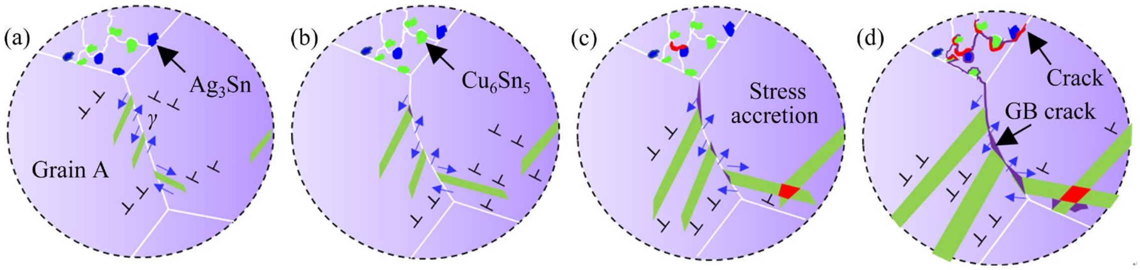

Fig. 10 Schematic diagrams illustrating premature brittle fracture behaviors at LNT: (a) Deformation twins nucleating from GBs; (b) Tensile deformation promoting growth of twins; (c) Stress concentration around secondary phases and TBs; (d) Cracks at TBs and secondary phases

5 Conclusions

(1) As the temperature declines, it is found that SAC305 solder alloy exhibits higher tensile strength and yield strength at LNT than at RT. In addition, deformation twins stabilize the strain hardening rate and the flow stress of the alloy.

(2) The fracture morphologies containing the intergranular fracture, some granular textures and transgranular fracture are observed at LNT. The alloy at RT displays ductile fracture feature with numerous dimples.

(3) The large velocity difference between twin thickening (~8 μm/s) and dislocation slip (~4 μm/s) leads to the premature fracture of the alloy. When the ambient temperature declines from RT to LNT, the fracture mechanism of SAC305 solder alloy changes from dislocation-dominated to deformation twin-dominated.

(4) It is found that secondary phases containing Cu_6Sn_5 and Ag_3Sn act as a precursor to the formation of cracks in the eutectic microstructure. Accordingly, crack propagation along the secondary phases leads to the failure of the alloy.

CRediT authorship contribution statement

Sheng-li LI: Writing − Original draft, Editing, Methodology, Investigation, Analysis, Software;

Chun-jin HANG: Writing − Review & editing, Supervision; **Qi-long GUAN:** Analysis; **Xiao-jiu TANG:** Supervision; **Ning ZHOU:** Analysis; **Yan-hong TIAN:** Investigation; **Wei ZHANG:** Editing, Analysis; **Dan YU:** Visualization; **Ying DING:** Analysis; **Xiu-li WANG:** Supervision.

Declaration of competing interest

The authors declare that they have no known competing financial interests or personal relationships that could have appeared to influence the work reported in this paper.

Acknowledgments

This work was supported by the National Natural Science Foundation of China (No. 51775141). Special thanks to HIT Center of Analysis Measurement and Computing (China) and Dr. Zhen ZHENG for the electron microscope test analysis.

Supplementary Information

Supplementary Information in this paper can be found at: http://tnmsc.csu.edu.cn/download/18-p1281-2023-0940-Supplementary_Information.pdf.

References

[1] WANG Meng, PENG Jian. Formation of ductile close-packed hexagonal solid solution on improving shear strength of Au−Ge/Cu soldering joint [J]. Transactions of Nonferrous Metals Society of China, 2023, 33: 2449−2460.

[2] LI Sheng-li, HANG Chun-jin, GUAN Qi-long, TANG Xiao-jiu, YU Dan, DING Ying, WANG Xiu-li. The microstructure evolution and failure mechanism of Sn37Pb solder joints under the coupling effects of extreme temperature variation and electromigration [J]. Materials Today Communications, 2023, 36: 106651.

[3] WU Ming, WANG Shan-lin, YIN Li-meng, CHEN Yu-hua, Hong Min, SUN Wen-jun, YAO Zong-xiang, NI Jia-ming, LU Peng, ZHANG Ti-ming, XIE Ji-lin. Oxidation behavior and intermetallic compound growth dynamics of SAC305/Cu solder joints under rapid thermal shock [J]. Transactions of Nonferrous Metals Society of China, 2023, 33: 3054−3066.

[4] WU Ming, WANG Shan-lin, SUN Wen-jun, HONG Min, CHEN Yu-hua, Ke Li-ming. Fracture pattern evolution of SnAgCu−SnPb mixed solder joints at cryogenic temperature [J]. Transactions of Nonferrous Metals Society of China, 2021, 31: 2762−2772.

[5] LI Sheng-li, LIU Yang, ZHANG Hao, CAI Hong-ming, SUN Feng-lian, ZHANG Guo-qi. Microstructure and hardness of SAC305 and SAC305−0.3Ni solder on Cu, high temperature treated Cu, and graphene-coated Cu substrates [J]. Results in Physics, 2018, 11: 617−622.

[6] JI Xiao-liang, AN Rong, ZHOU Wei, ZHONG Ying, GUO Fu, WANG Chun-qing. Revealing the ductile-to-brittle transition mechanism in polycrystalline body-centered tetragonal tin (Sn) for cryogenic electronics [J]. Journal of Alloys and Compounds, 2022, 903: 163948.

[7] LI Sheng-li, HANG Chun-jin, ZHANG Wei, GUAN Qi-long, TANG Xiao-jiu, YU Dan, DING Ying, WANG Xiu-li. Current-induced solder evolution and mechanical property of Sn−3.0Ag−0.5Cu solder joints under thermal shock condition [J]. Journal of Alloys and Compounds, 2024, 970: 172519.

[8] FINK M, FABING Th, SCHEERER M, SEMERAD E, DUNN B. Measurement of mechanical properties of electronic materials at temperatures down to 4.2 K [J]. Cryogenics, 2008, 48: 497−510.

[9] JONES W K, LIU Yan-qing, SHAH M, CLARKE R. Mechanical properties of Pb/Sn Pb/In and Sn−In solders [J]. Soldering and Surface Mount Technology, 1998, 10: 37−41.

[10] TIAN Ru-yu, HANG Chun-jin, TIAN Yan-hong, WU Bing-ying, LIU Yu-bin, ZHAO Jie. Interfacial intermetallic compound growth in Sn−3Ag−0.5Cu/Cu solder joints induced by stress gradient at cryogenic temperatures [J]. Journal of Alloys and Compounds, 2019, 800: 180−190.

[11] YAN Chen-kan, FENG Ai-han, QU Shou-jiang, CAO Guo-jian, SUN Jing-li, SHEN Jun, CHEN Dao-lun. Dynamic recrystallization of titanium: Effect of pre-activated twinning at cryogenic temperature [J]. Acta Materialia, 2018, 154: 311−324.

[12] KANLAYASIRI K, MOOKAM N. Influence of Cu content on microstructure, grain orientation and mechanical properties of Sn–*x*Cu lead-free solders [J]. Transactions of Nonferrous Metals Society of China, 2022, 32: 1226−1241.

[13] STEPANOV N D, SHAYSULTANOV D G, CHERNICHENKO R S, YURCHENKO N Y, ZHEREBTSOV S V, TIKHONOVSKY M A, SALISHCHEV G A. Effect of thermomechanical processing on microstructure and mechanical properties of the carbon-containing CoCrFeNiMn high entropy alloy [J]. Journal of Alloys and Compounds, 2017, 693: 394−405.

[14] HAN Jing, SUN Jian, WEN Ting-yu, GUO Fu. Analysis of continuous recrystallization (sub)grain rotation behavior in Pb-free solder bumps under a 0.1 μm/s shear rate [J]. Journal of Materials Science: Materials in Electronics, 2018, 29: 10992−10999.

[15] JI Xiao-liang, WANG Li-hua, XIA Yi-ping, GUO Fu, WANG Chun-qing. Enhance cryogenic ductility and strength of body-centered tetragonal Sn by pre-twinning and recrystallization [J]. Materials Science and Engineering A, 2023, 888: 145810.

[16] LI Sheng-li, HANG Chun-jin, ZHANG Wei, TIAN Yan-hong, YU Dan, DING Ying, WANG Xiu-li. Fracture behavior and constitutive relations of Sn−3.0Ag−0.5Cu solder alloy at cryogenic temperature [J]. Materials Science and Engineering A, 2024, 896: 146280.

[17] LAPLANCHE G, KOSTKA A, HORST O M, EGGELER G, GEORGE E P. Microstructure evolution and critical stress for twinning in the CrMnFeCoNi high-entropy alloy [J]. Acta Materialia, 2016, 118: 152−163.

[18] KONDO S, MITSUMA T, SHIBATA N, IKUHARA Y. Direct observation of individual dislocation interaction processes with grain boundaries [J]. Science Advances, 2016,

2: e1501926.

[19] KOU Zong-de, YANG Yan-qing, YANG Li-xia, HUANG Bin, LUO Xian. Twinning-assisted void initiation and crack evolution in Cu thin film: An in situ TEM and molecular dynamics study [J]. Materials Science and Engineering A, 2018, 737: 336−340.

[20] HUANG Zhao-wen, JIN Shen-bao, ZHOU Hao, LI Yu-sheng, CAO Yang, ZHU Yun-tian. Evolution of twinning systems and variants during sequential twinning in cryo-rolled titanium [J]. International Journal of Plasticity, 2019, 112: 52−67.

[21] MIRACLE D B, SENKOV O N. A critical review of high entropy alloys and related concepts [J]. Acta Materialia, 2017, 122: 448−511.

[22] GEORGE E P, CURTIN W A, TASAN C C. High entropy alloys: A focused review of mechanical properties and deformation mechanisms [J]. Acta Materialia, 2020, 188: 435−474.

[23] JOO S H, KATO H, JANG Min-ji, MOON J, TSAI C W, YEH J W, KIM H S. Tensile deformation behavior and deformation twinning of an equimolar CoCrFeMnNi high-entropy alloy [J]. Materials Science and Engineering A, 2017, 689: 122−133.

[24] LU Kai-ju, CHAUHAN A, LITVINOV D, TIRUNILAI A S, FREUDENBERGER J, KAUFFMANN A, HEILMAIER M, AKTAA J. Micro-mechanical deformation behavior of CoCrFeMnNi high-entropy alloy [J]. Journal of Materials Science Technology, 2022, 100: 237−245.

[25] BHATIA M A, ADLAKHA I, LU Gang, SOLANKI K N. Generalized stacking fault energies and slip in β-tin [J]. Scripta Materialia, 2016, 123: 21−25.

[26] ZAMBALDI C, RAABE D. Plastic anisotropy of γ-TiAl revealed by axisymmetric indentation [J]. Acta Materialia, 2010, 58: 3516−3530.

[27] JO Y H, CHOI W M, SOHN S S, KIM H S, LEE B J, LEE S. Role of brittle sigma phase in cryogenic-temperature-strength improvement of non-equi-atomic Fe-rich VCrMnFeCoNi high entropy alloys [J]. Materials Science and Engineering A, 2018, 724: 403−410.

[28] PARK J M, MOON J, BAE J W, KIM D H, JO Y H, LEE S, KIM H S. Role of BCC phase on tensile behavior of dual-phase Al0.5CoCrFeMnNi high-entropy alloy at cryogenic temperature [J]. Materials Science and Engineering A, 2019, 746: 443−447.

[29] XIAN J W, ZENG G, Belyakov S A, GU Q, NOGITA K, GOURLAY C M. Anisotropic thermal expansion of Ni_3Sn_4, Ag_3Sn, Cu_3Sn, Cu_6Sn_5 and βSn [J]. Intermetallics, 2017, 91: 50−64.

[30] BILLAH M M, SIDDIQUEE R I, MOHAMMAD M, PAUL R, RABBI M S. Effects of temperature and strain rate on tensile properties of (Ag,Cu)-Sn intermetallic compounds: A molecular dynamics study [J]. Journal of Materials Research and Technology, 2022, 18: 3044−3055.

[31] MARUYAMA S. Dynamic behaviour of twinning in tin crystals at various temperatures and strain rates [J]. Journal of the Physical Society of Japan, 1960, 15: 1243−1251.

极端温度下 Sn−3.0Ag−0.5Cu 钎料合金韧脆转变机制

李胜利[1]，杭春进[1,2]，关旗龙[1]，唐晓玖[1]，周 宁[1]，田艳红[1]，张 威[1]，于 丹[3]，丁 颖[3]，王修利[3]

1. 哈尔滨工业大学 材料结构精密焊接与连接国家重点实验室，哈尔滨 150001；
2. 哈尔滨工业大学 郑州研究院，郑州 450041；
3. 北京控制工程研究所，北京 100094

摘　要：通过不同温度下的单轴拉伸实验，研究了液氮温度(LNT，77 K)下 Sn−3.0Ag−0.5Cu(SAC305)焊料合金的固有脆断行为和韧脆性转变(DBT)机制。与 SAC305 焊料合金在室温(RT, 293 K)下由动态恢复和动态再结晶激活的软化过程相比，嵌入体心四方 Sn 中的相交和非相交变形孪晶可提高合金抗拉强度并稳定应变硬化率，但降低合金的伸长率。孪晶增厚(约 8 μm/s)和位错滑移(约 4 μm/s)之间不可调和的速度差导致在线性硬化过程中过早出现脆性断裂，使合金发生韧脆性转变。此外，第二相削弱 SAC305 钎料合金的力学性能，并于 Cu_6Sn_5 和 Ag_3Sn 之间形成微裂纹。

关键词：SAC305；变形孪晶；第二相；拉伸性能；极端温度

(Edited by Bing YANG)